Chapter 6

Abrasion-Corrosion of Ferritic Stainless Steel

Wilian S. Labiapari, Miguel A. N. Ardila,
Henara L. Costa and José Daniel B. de Mello

Additional information is available at the end of the chapter

http://dx.doi.org/10.5772/intechopen.81913

Abstract

Several studies have measured abrasion-corrosion for biomaterials, alloys, and stainless steel. Despite the considerable effort to understand the synergy between abrasion-corrosion resistance of stainless steel, they have mainly focused on more traditional materials, such as AISI 304 and AISI 316 stainless steel, and, more recently, on AISI 2205 duplex stainless steel. Little progress has been made to understand this phenomenon for cost-effective ferritic stainless steel. In this chapter, we first show the great potential of the use of ferritic stainless steel in the sugar cane biofuel industry. The influence of their crystallographic texture on the corrosion resistance of 16% Cr ferritic stainless steel (both niobium-stabilized and non-stabilized) is presented and discussed. We also analyses the microabrasion-corrosion performance of ferritic stainless steel with different chemical compositions (11%wt Cr with and without Ti stabilization; 16%wt Cr with and without Nb stabilization) and, for comparative purposes, austenitic stainless steel (18%wt Cr-8%wt Ni) and carbon steel (0.2%wt C). For all materials tested, microabrasion wear coefficients were higher (4x) than those measured under abrasion-corrosion conditions. Friction coefficients could also be measured by a 3D load cell strategically positioned in the specially developed microabrasion-corrosion device, showing a strong reduction (2x) in friction coefficient under abrasion-corrosion conditions when compared with solely abrasion conditions.

Keywords: ferritic stainless steel, abrasion-corrosion, synergy, force measurements, friction coefficient, potentiodynamic polarization, crystallographic texture, Ti and Nb stabilization, biofuel industry

1. Introduction

In various engineering applications, mechanical components are simultaneously subjected to a combination of mechanical wear and corrosion [1, 2]. Due to their high corrosion resistance, stainless steel could be an interesting candidate, despite its relatively low mechanical

resistance when compared to other hard wear-resistant materials. For example, in conditions of moderate corrosion in combination with mechanical wear, such as in the initial stages of sugar cane plants for ethanol production, a previous work proved an exceptional performance of inexpensive ferritic stainless steel at low cost-benefit ratios [3].

The corrosion resistance of stainless steel is attributed to the formation of a protective passivated layer, and they are generally regarded as materials that are easily repassivated. The dynamics involving the removal of the passive layer by mechanical action and repassivation plays an important role in the abrasion-corrosion resistance of stainless steel. The complex tribochemical mechanisms of stainless steel depend on the microstructure and chemical composition of the material surface, the solution pH, the abrasive (size, type and concentration) and the imposed electrochemical conditions [4].

Most studies about abrasion-corrosion resistance of stainless steel are mainly focused on more traditional materials, such as AISI 304 and AISI 316 stainless steel, and, more recently, on AISI 2205 duplex stainless steel. The investigation of cost-effective ferritic stainless steel for those applications is often neglected. Despite this, they have found an important application niche in the biofuel industry [3], which certainly involves abrasion and corrosion. Within ferritic stainless steel, it is relevant to investigate the effect of Cr content on tribocorrosion, as well as the effect of stabilization. The cheapest stainless steel is 11Cr (DIN 14003), and it has vast application in the sugar cane biofuel industry. 11CrTi (ASTM S40910) is also a low-cost ferritic stainless steel stabilized with Ti, largely used in automobile exhaust systems. 16Cr (ASTM S43000) steel is a slightly more expensive ferritic stainless steel, mainly used in the cutlery industry, but it is still cheaper than austenitic steel. 16CrNb (ASTM S43000) is the same 16Cr stainless steel stabilized with Nb used in cutlery and stamping. On the other hand, austenitic stainless steel, such as 18Cr8Ni (AISI 304), presents higher cost, but is extremely versatile in its use, with high corrosion resistance, good formability and weldability.

The abrasion and corrosion phenomena have become of great importance in sectors where the contact between two surfaces in relative motion and the chemically reactive environment are the main failure factors. Thus, several methodologies and tests have been developed to study the mechanisms that originate the phenomena of abrasion and corrosion separately; but in the industry, the phenomena of abrasion and corrosion happen simultaneously. Some examples of such occurrences are pumps, process valves, oil-gas pipelines in the marine industry and metal surgical implants replacing bone parts of the human body [1]. With advances in the understanding of abrasion and corrosion, independently treated, the interest and necessity of studying the microabrasion interactions in aqueous conditions arose, especially when the environment is corrosive [1, 2].

In systems where corrosion and mechanical wear co-occur, phenomena such as plastic deformation not only influence mechanical failure due to wear, but also lead to the removal of passivation layers present on the metal surface. Exposed metal surfaces can be highly reactive to the environment, which can accelerate corrosion [5].

The combined effect of abrasion and corrosion, the so-called synergistic effect, has been widely debated in the literature. Corrosion has been shown to accentuate abrasion [2, 4, 6–9],

http://dx.doi.org/10.5772/intechopen.81913

while for others abrasion is attenuated by corrosion [7, 9]. However, even though considerable efforts have been made to understand the synergy between abrasion and corrosion, little progress has been made in quantifying this phenomenon for stainless steel [6].

2. Ferritic stainless steel as an antiwear material for the biofuel industry

Society and governments have been highly interested in a large-scale production of alternative forms of energy, such as biofuels, which reduce greenhouse gas emissions and improve energy security when compared to their fossil counterparts. As a successful example, the vast majority of automotive cars in Brazil (86%) are manufactured with engines that can use any amount of gasoline or ethanol, a technique called flex-fuel [10]. One of the most productive sources of ethanol is sugar cane. The energy matrix based on biofuels in Brazil started in the 1980s [11], when the production of ethanol was 2500 l/hectare. Nowadays, the production is 6500 l/hectare and it is expected to reach 13,000 l/hectare in 2020. With increased production and efficiency, the period available for the annual plant maintenance has been drastically reduced. One of the main reasons for the annual maintenance is premature wear of devices used to wash, cut and crush sugar cane. In general, the main material used in sugar cane plants is structural steel with low carbon content. The main rational for this choice is the material's low cost, although its good weldability is also an important factor. It is expected that abrasive wear will occur, mainly due to the presence of cane husk, soil and sand present in the cane, but that the severity of abrasive wear will be moderate. Therefore, the wear life of the components should allow them to last for the whole sugar cane season, and their majority would be replaced for the next season. Corrosion in the components used to receive, wash, cut, shred and mill sugar cane could be relevant both during season and during off-season. During season, corrosion due to humidity and water (cane washing, rain, dew, added water, etc.) could occur concomitantly with abrasive wear due to cane husk, soil and sand particles transported with the cane and the synergy between abrasion and corrosion should be investigated. During off-season, corrosion due to humidity and water (rain, dew) probably does not passivate carbon steel and leads to irregular surfaces with corrosion products, which will then be subsequently removed by abrasive wear in the next season.

A recent paper proposed and evaluated an alternative solution for the biofuel industry [3]. It investigates the use of low-cost ferritic stainless steel in real tribocorrosive systems subjected to corrosion due to water and moderate abrasive wear simultaneously. The first step was a pioneer introduction of stainless steel in some components used in the initial stages of sugar cane processing, motivated by corrosion that was easily observed in the components during off-season.

A visual comparison between carbon steel (A36) and ferritic stainless steel (P410) is shown in **Figure 1**, where cane transportation conveyors made of the two materials are compared. Since the samples were collected during season, the movement of the cane on the surfaces helps to clean corrosive products and, therefore, both surfaces appear smooth and clean. However, a

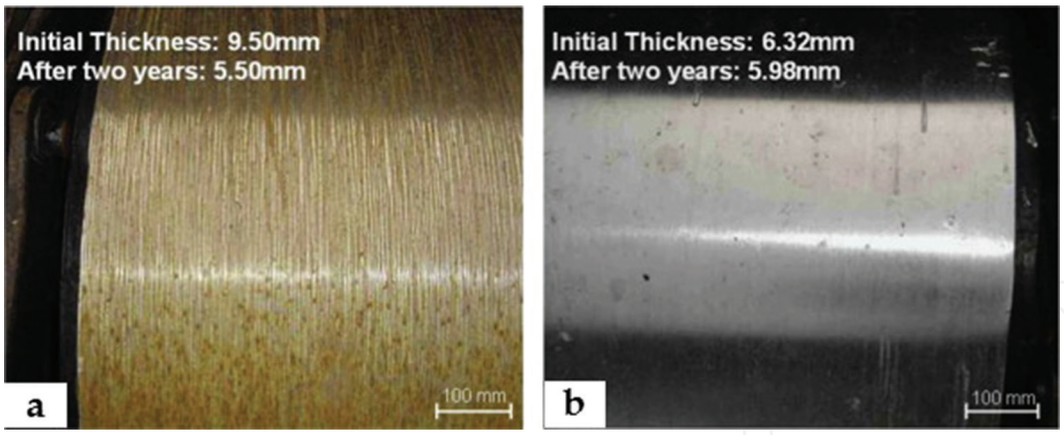

Figure 1. Worn surfaces in cane transport conveyors during field tests after use during two seasons: (a) A36 and (b) P410D [3].

yellow coloration can be observed for carbon steel because the samples are presented after 24 h of maintenance, showing that even during a shortstop, corrosion products begin to accumulate for carbon steel [12].

In addition, the wear measured by the reduction in thicknesses of the carbon steel and ferritic stainless steel sheets installed in similar components is summarized in **Figure 2**. The dotted lines refer to the thickness reduction of a carbon steel sheet and the complete lines refer to ferritic stainless steel sheet. The superior performance of stainless steel is clearly evidenced, where the thickness reduction was minimal. The locations 1, 2, 3 and 4 indicated in this figure relate to the four positions along the sheet [3].

The change to ferritic stainless steel also influenced the quality of the sugar produced. The introduction of ferritic stainless steel in sugar cane industries started only for a few components in 2003 and gradually increased until 2007, so that in 2007 the vast majority of the

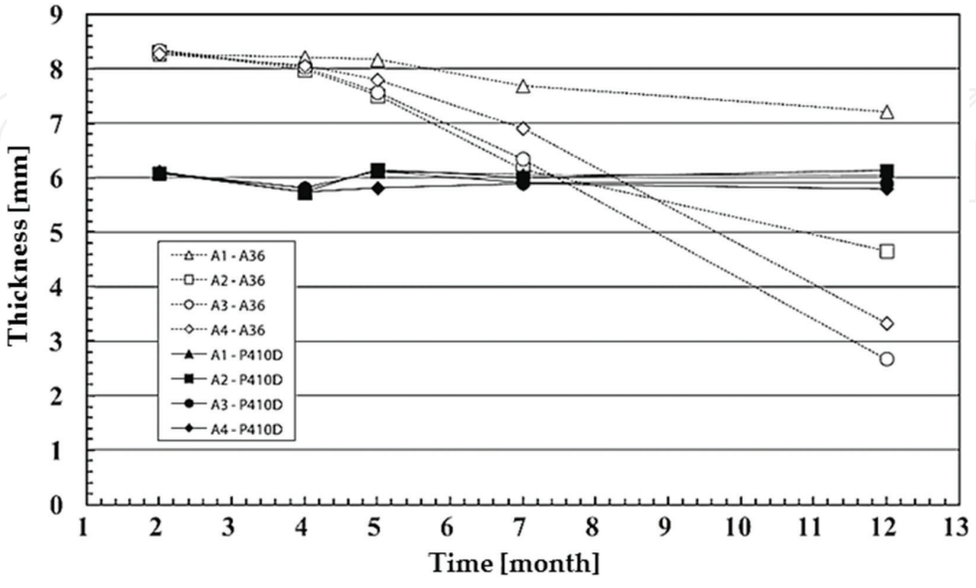

Figure 2. Thickness reduction of carbon steel and stainless steel plates during 10 months of use in field tests [3].

http://dx.doi.org/10.5772/intechopen.81913

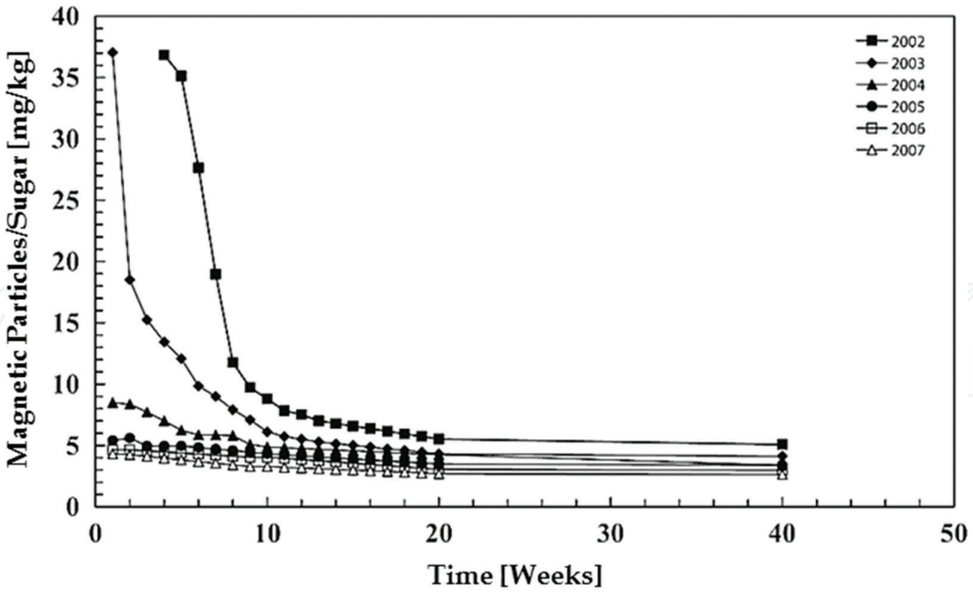

Figure 3. Evolution of the amount of magnetic particles in sugar produced between 2002 and 2007 [3].

components used to receive sugar cane and move it to the processing line were replaced by steel stainless. **Figure 3** shows the comparison of the evolution of the weight of magnetic particles in the final product due to wear debris between the years of 2002 and 2007. This figure clearly shows that before 2003, a few weeks of use were necessary to significantly reduce the number of debris in the final product, while in 2007, good quality sugar (without metallic wear debris) could be produced in the first week of use [3].

Carbon steel parts (which have been gradually reduced from 2003) can suffer severe corrosion during off-season or maintenance stops because carbon steel does not passivate [12, 13]. Corroded areas will likely become preferred locations for abrasive wear and the synergy between abrasion and corrosion will lead to severe material removal. When carbon steel was completely replaced by stainless steel (2007), the corrosion products accumulated during the off-season could be removed in the first week of use, for the passivation protects the surface against corrosion caused by rain, dew, etc. The authors [3] point out that when carbon steel is used, even after reduction to a much smaller level, the amount of metal debris in the final sugar is still significantly higher than when stainless steel is used, which shows a synergy between abrasion and corrosion also during season, when the sliding of the surfaces continuously removes possible products of corrosion [3].

3. Influence of crystallographic texture and niobium stabilization on the corrosion resistance of ferritic stainless steel

Previous studies reported that after hot and cold rolling processes, stainless steel showed preferential crystallographic textures [14–20]. In particular, Raabe and Lücke [17] showed that ferritic steel, both non-stabilized and stabilized with Nb or Ti, had a texture gradient throughout the thickness of the samples. It was observed that the magnitude of the Goss shear texture

varied with the position throughout the thickness, specially prevailing at 20% depth from the sheet surface. The Goss texture occurs as a recrystallization texture for FCC materials. For ferritic steel AISI 430 with different Nb content, new crystallographic texture components appear and these are attributed to the formation of coarse grains when niobium content varies [21]. Crystallographic texture analyses were performed in a conventional "Electron Backscatter Diffraction" (EBSD) system attached to a SEM. **Figure 4** exemplifies, using EBSD analysis, the crystallographic texture distribution throughout the thickness of AISI 430 rolled ferritic stainless steel with (16CrNb) and without Nb (16Cr) stabilization (see **Table 1** for chemical composition). The ferritic stainless steel samples' thickness was 4 mm. **Figure 4a** shows the scheme used for extraction of steel samples from the regions defined as surface and centre.

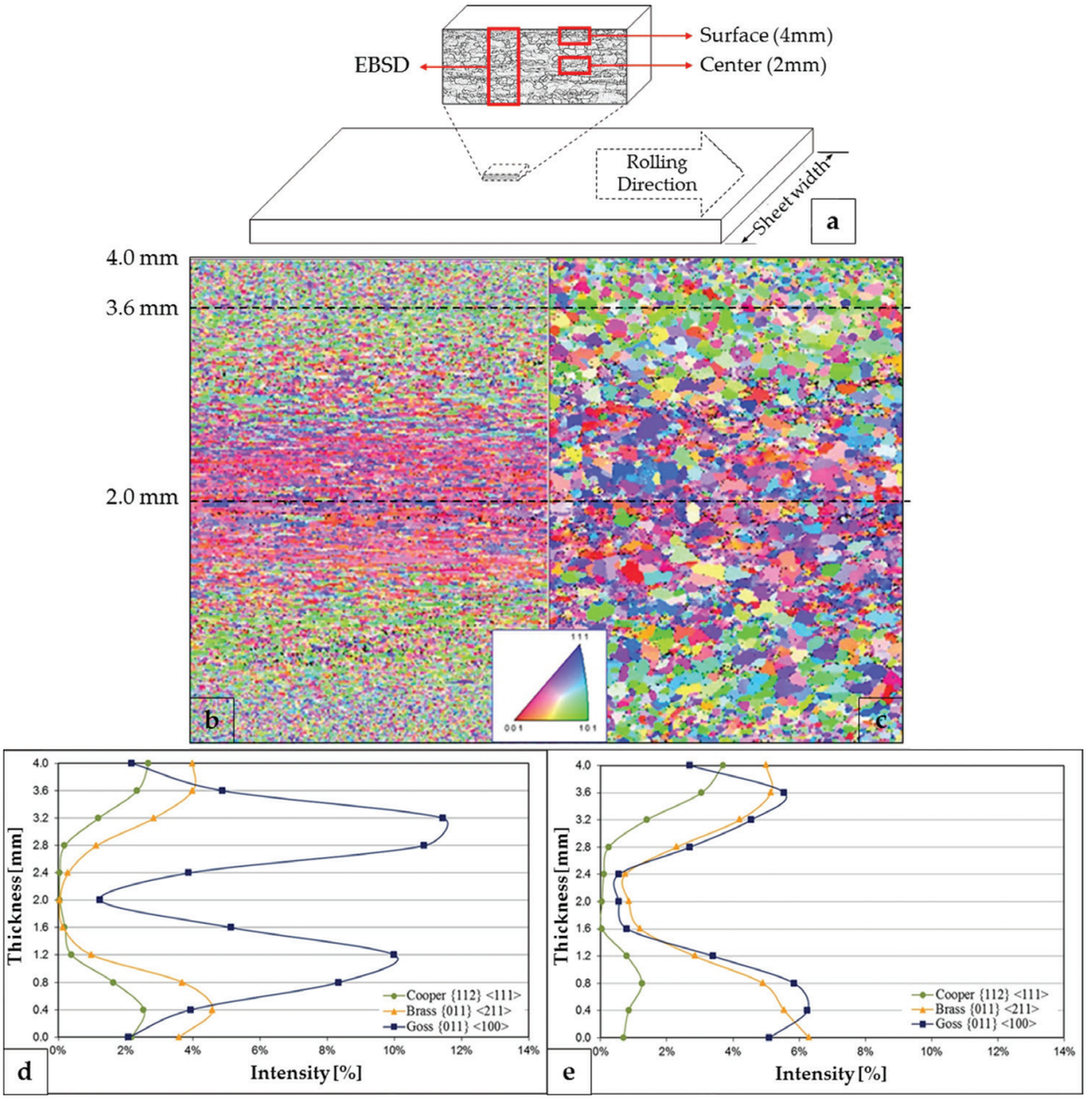

Figure 4. EBSD analysis of a 16Cr ferritic stainless steel with and without Nb stabilization: (a) Scheme of sample extraction; Inverse pole figure: (b) 16Cr, (c) 16CrNb; Texture intensity through the thickness: (d) 16 Cr, (e) 16 CrNb.

http://dx.doi.org/10.5772/intechopen.81913

Element (%wt)	11Cr	11CrTi	16Cr	16CrNb	17CrTiNb	18Cr8Ni	A36
C	0.011	0.009	0.049	0.025	0.011	0.055	0.138
Mn	0.61	0.13	0.32	0.21	0.16	1.15	1.06
Si	0.49	0.52	0.36	0.46	0.36	0.42	0.01
P	0.0247	0.0182	0.0395	0.0358	0.0219	0.0251	0.0154
S	0.0002	0.0005	0.0015	0.0013	0.0024	0.0009	0.0075
Cr	11.23	11.29	16.10	16.19	17.62	18.28	0.01
Ni	0.31	0.12	0.27	0.19	0.17	8.01	0.01
Mo	0.021	0.005	0.020	0.035	1.75	0.063	0.003
Al	0.002	0.003	0.002	0.002	0.0055	0.003	0.033
Nb	0.006	0.002	0.014	0.416	0.183	0.005	0.001
Ti	0.003	0.144	0.003	0.004	0.177	0.001	0.001
N	0.0145	0.0087	0.0528	0.0202	0.0112	0.0421	0.0026

Table 1. Chemical composition of the specimens.

The inverse pole figures obtained for the EBSD texture analyses are given in **Figure 4b** and **c**. It can be seen that 16Cr samples show a larger texture gradient throughout their thickness when compared to 16CrNb samples. On the surface, the preferential orientations are <101> and <111>, whereas in the centre, they are <001> and <111>. It was also inferred that the 16CrNb steel has larger grains than the 16Cr steel. However, Ardila et al. [21] argued that the difference in grain size between 16Cr and 16CrNb steel had no influence on pitting potential.

For a quantitative description of the crystalline orientations, a crystalline orientation distribution function (CODF) was used. Only shear textures were considered, see **Figure 4d** and **e**. It can be seen that the 16Cr and 16CrNb steel have similar textures at positions that corresponded to different thicknesses (4, 3.6 and 2 mm). It is also observed that in the centre of the plate (position corresponding to 2 mm), there are no relevant shear textures—all have intensities lower than 1%. The principal shear texture at the position corresponding to 3.6 mm was Goss 011 <100> with intensity 4.9% for the 16Cr and 5.5% for the 16CrNb steel. It can also be observed that the shear texture brass 011<211> is more intense closer to the surface (position corresponding to 4 mm). This is due to the recrystallization taking place preferentially at the metal surface and can be explained by the plastic deformation generated during this phenomenon. Deformation is influenced by the presence of alloying elements such as niobium [17, 20, 22], and explains the slightly high intensity of the brass texture for steel 16CrNb (5%) compared to the steel 16Cr (4%). The copper shear texture 112<111>/shear texture Goss 011<111> was present with similar intensity at the positions corresponding to the surface (4 mm) and 3.6 mm, with approximately 2.50% for the 16Cr steel and 3.35% for the 16CrNb steel. The Goss texture also prevails in the 16Cr steel, but its highest intensity occurs at the thickness of 3.2 mm (65% from the centre to the surface), although at 3.6 mm the values are also high. The difference in intensity throughout the thickness may be caused by the stabilization with niobium [17, 20, 22], and also by the grain

size [22]. Summarizing, the shear texture Goss 011 <100> is the most important texture variation between the surface (4 mm) and the bulk of the plate. For both materials, the fibre texture was little affected by the position [19]. As a consequence, we may suppose that variation in properties is governed by the presence of Goss texture with greater intensity at 3.6 mm.

To verify the influence of the crystallographic texture on corrosion resistance, the pitting potentials were measured using samples taken from the same plate for each steel at the positions corresponding to 4, 3.6 and 2 mm, as indicated in **Figure 4a**. Typical results of the anodic potentiodynamic polarization curves (obtained according to ASTM standard G59-97 [23] in a 3.56% NaCl electrolyte) are presented in **Figure 5**.

The 16CrNb steel presented higher pitting resistance than 16Cr steel. The carbon content of 16Cr steel is higher than that of 16CrNb steel (**Table 1**). In this way, 16Cr steel is more susceptible to the formation of Cr carbides, mainly at the grain boundaries. In addition, in the steel stabilized with Nb, carbon will preferentially form Nb carbides instead of Cr carbides, thus decreasing Cr depletion in the matrix [24]. Higher Cr-free content in stainless steel benefits the formation of more stable passive films on the steel surface, which prevents the penetration of chloride and sulfate ions. Consequently, Cr enhances pitting corrosion resistance and uniform corrosion resistance [25]. Moreover, Nb contributes to corrosion resistance when it is added to the alloy [26–29], the addition of this element in ferritic stainless steel changes the characteristics of the surface film of oxide semiconductor caused by Nb^{5+} incorporation into the passive layer. This fact shifts the current to lower values, and results in increased pitting corrosion resistance [26, 29].

Additionally, the pitting potential increases at the position corresponding to 3.6 mm and decreases at the center of the sample (2 mm), that is, the corrosion resistance is lower at the centre. Ardila et al. [21] reported that the orientation of the fibre textures <110> (α, ζ and ε fibers) was predominant for both steel specimens throughout the thickness, whereas the shear texture (Goss) with orientation <100> appeared predominantly at 3.6 mm (**Figure 4**). It is reasonable to suppose that the presence of the orientation <100> in the shear texture is at the origin of the improvement of pitting resistance in ferritic steel, which has higher atomic density intrinsic of the cubic crystalline systems [30–32]. Previous studies [32, 33] showed that

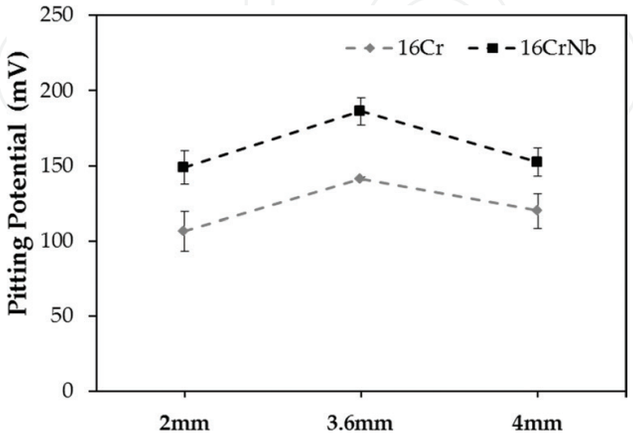

Figure 5. Pitting potential during standard corrosion tests as a function of thickness in 16Cr ferritic stainless steel, with and without Nb stabilization [21].

the lower susceptibility to pitting is related to increasing atomic density planes of the FCC system, with this susceptibility decreasing in the following order: 110 > 100 > 111. The crystallographic planes with a high number of nearest neighbor atoms require higher total energy for the breaking of the bonds and the subsequent dissolution of atoms [34].

Figure 6 shows typical surfaces after anodic potentiodynamic polarization tests in 1 N H_2SO_4. It is clear that for the 16CrNb steel samples, the severity of corrosion allowed a neat visualization of

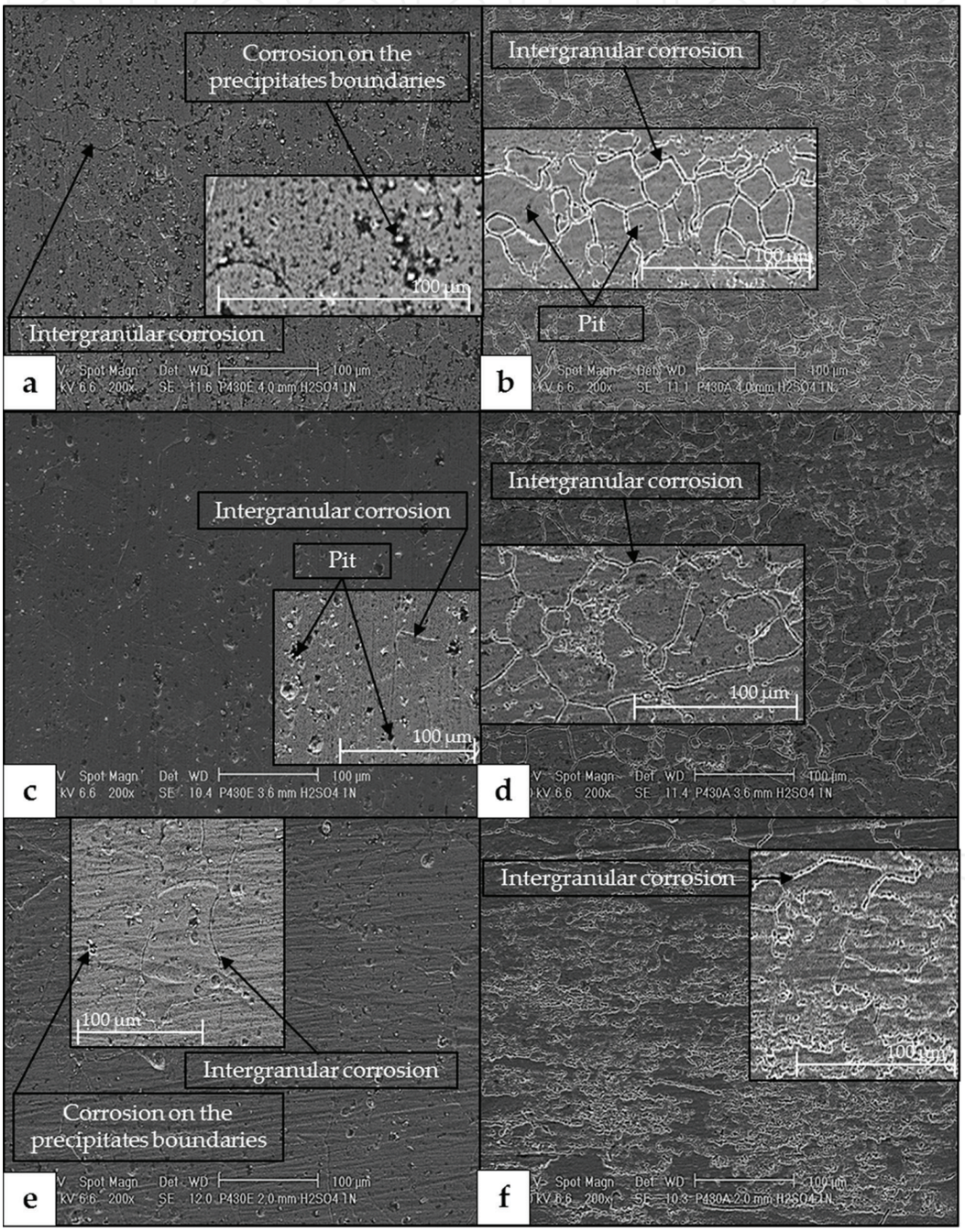

Figure 6. SEM images of the ferritic stainless steel samples tested throughout the thickness in 1 N H_2SO_4. (a) 16CrNb 4 mm; (b) 16Cr 4 mm; (c) 16CrNb 3.6 mm; (d) 16Cr 3.6 mm; (e) 16CrNb 2 mm; (f) 16Cr 2 mm [21].

niobium carbides, whereas for the 16Cr steel samples, intergranular corrosion was more prevalent, which agreed well with previous results regarding corrosion phenomena in 16CrNb and 16Cr steel. Niobium carbide precipitates were observed throughout the surface of the 16CrNb steel samples as white spots. At 4 and 2 mm, weak granular corrosion was identified (**Figure 6a** and **e**), as well as more substantial corrosion at the boundaries of the carbides, a phenomenon that was not detected at 3.6 mm (**Figure 6c**). At this position, in addition to a small amount of intergranular corrosion, a slight presence of pits was observed, but it cannot be concluded that the corrosion is significant there. For 16Cr steel, intergranular corrosion was observed throughout the thickness, although at the surface (position corresponding to 4 mm), some pits could be observed inside the grains (**Figure 6b**). Compared to the centre of the samples, that is, at 2 mm (**Figure 6f**), a significant amount of intergranular corrosion was observed, as well as a generalized degradation of the surface that can be considered generalized corrosion.

4. Microabrasion-corrosion of ferritic stainless steel

With the basic understanding of the influence of systemic factors on the electrochemical corrosion of ferritic stainless steel, the understanding of the influence of abrasion on corrosion and vice versa can be discussed. For this, an "in situ" technique that simultaneously assesses abrasion and corrosion was developed, and with that, a test rig that joins the techniques of microabrasion and electrochemical corrosion was developed [2, 35–40]. The principle is to install an electrochemical cell in a fixed-sphere microabrasive test rig; the cell is connected to a potentiostat for the potential difference application, as exemplified in **Figure 7**. One of the latest hybrid abrasion-corrosion test rigs combined an electrochemical cell and a potentiostat with a fixed ball microabrasion tester [38], and in this way, the contact forces (normal and frictional forces) were monitored in real time. A schematic view of this test rig is shown in **Figure 8**. The equipment can be divided into four parts:

- **Abrasive slurry preparation:** It consists of an electromagnetic mixer that guarantees the homogeneity of the solution and a peristaltic pump to sustain a controlled flow of the slurry during the test. The slurry is a mixture of the abrasive particles and the electrolytic medium.
- **Image acquisition and processing system**: A digital camera ensures the measurement of the wear scar which is analysed by an image processing software.
- **Motion and loading measurements**: The load can be applied using dead weight or an electromagnetic actuator; therefore, it is possible to run a test with a fixed normal load or a variable controlled load. This latter characteristic is quite unique because it allows the comparison of wear behavior under constant load and constant pressure. The force is transmitted from its point of application to the sample by a lever arm system. A three-dimensional load cell (measuring three forces and three moments simultaneously) was installed after the lever arm. In order to protect the load cell against corrosion, it was positioned outside the electrochemical cell and the load was transmitted, using a polymeric rod, through a flexible membrane acting as a cell wall. The flexible membrane poses negligible mechanical

http://dx.doi.org/10.5772/intechopen.81913

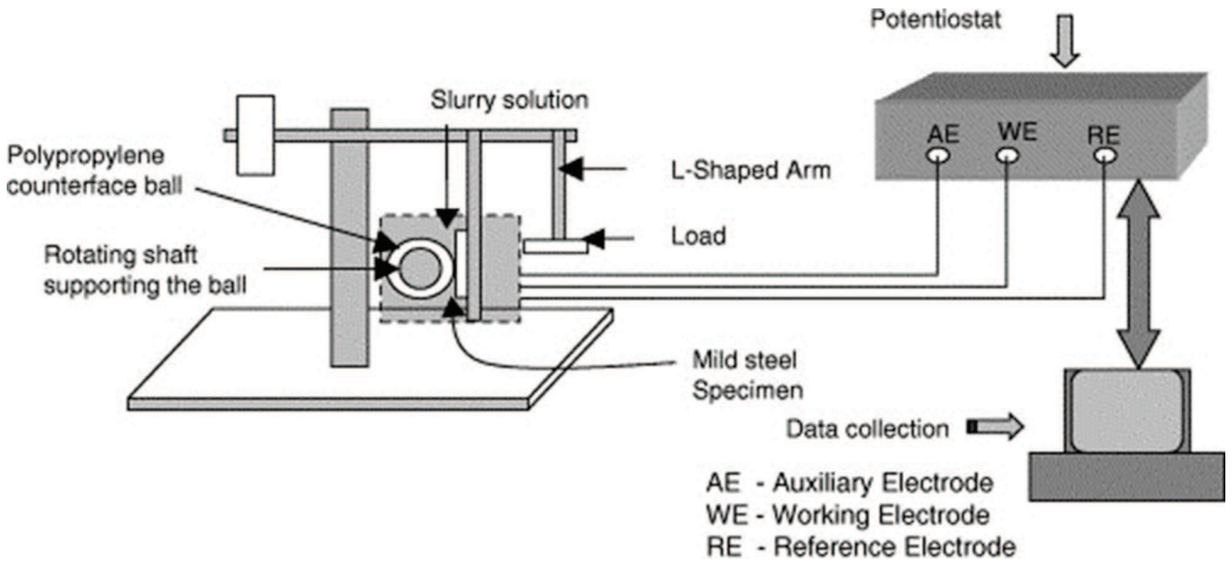

Figure 7. Schematic drawing of the adaptation of the microabrasion test for abrasion-corrosion tests [2].

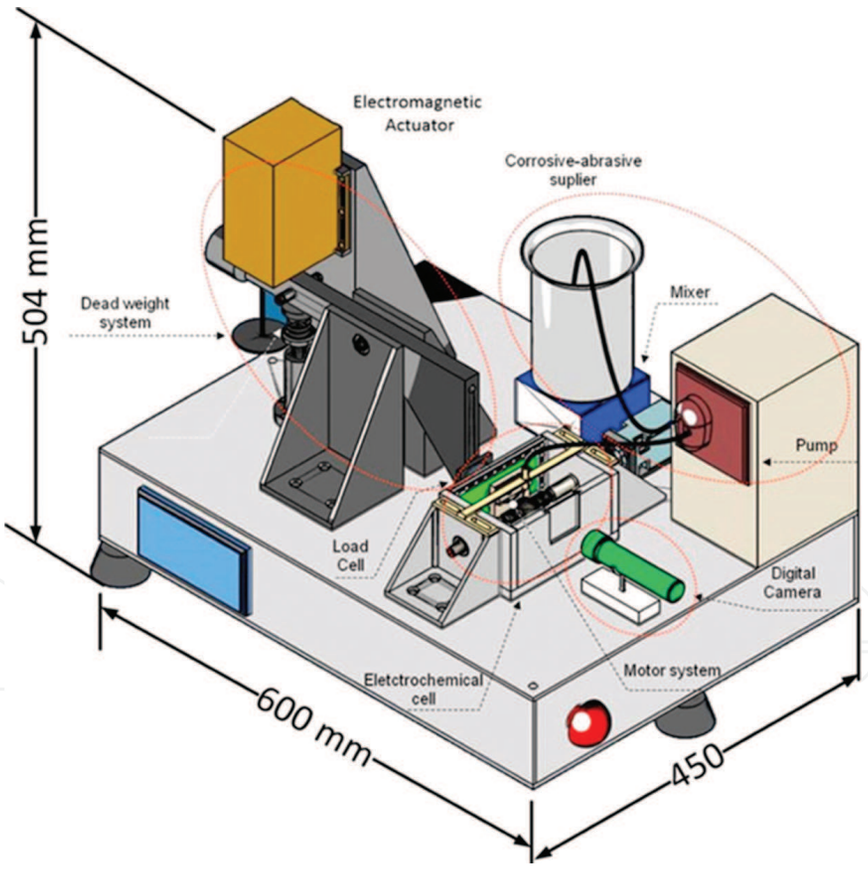

Figure 8. Schematic drawing of the test rig with monitoring of the contact forces (normal and frictional forces) in real time [38].

interference on the load transmission while assuring a watertight and insulated electrochemical cell. The rotary speed of the sphere is assured by a DC motor controlled using a closed loop methodology, where the velocity feedback signal is provided by a quadrature

encoder. The possibility of monitoring the efforts throughout the test is a differential in relation to other test rigs reported in the literature.

- **Electrochemical cell**: The electrodes from a Biologic potentiometer, model SP-150, had been positioned within the electrochemical cell, which is made of methyl methacrylate, at a constant level of electrolyte, which assures electrical contact between all electrodes.

The development of these test rigs allows the comparison of the polarization curves in pure corrosion and abrasion-corrosion tests. **Figure 9** exemplifies this comparison for 16CrNb ferritic stainless steel.

The corrosion test conditions were similar to the conditions described in the tests reported in **Figure 5**, that is, they have been aerated and partially submerged and used a saline bridge (turbulent). For the same electrochemical parameters, an increase in the passive current density was observed in the abrasion-corrosion tests when compared with the pure corrosion tests.

This increase in passivation current density is attributed to the dynamics involved in passive layer removal and repassivation [2, 4, 41]. The slight increase in current density in the "passivation region" reflects a less effective repassivation [36]. Evidence of this constant removal and generation of the passive layer is the fluctuation (noise) observed in the current density in the abrasive-corrosive tests when compared with corrosive tests. The fluctuation in the current is due to spontaneous repassivation within the wear scar and subsequent depassivation due to the action of abrasive particles [4]. During the sliding wear of passive metals, the abrupt variation (noise) of the anodic current corresponds to the rate of electrochemical removal of the metal in the wear mark [42].

This chapter analyses the microabrasion-corrosion performance of ferritic stainless steel with different chemical compositions, in particular Cr content:

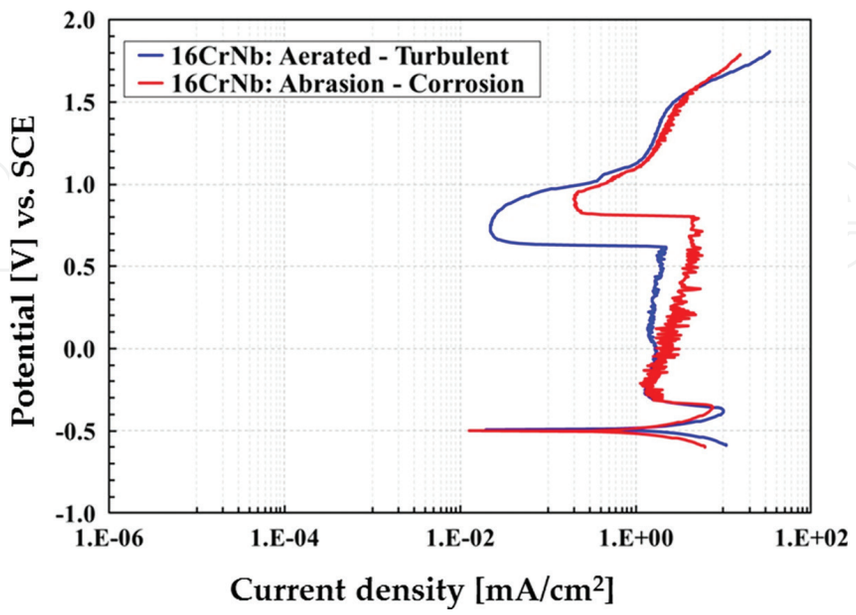

Figure 9. Typical potentiodynamic polarization curves for 16CrNb stainless steel [36].

- 11%wt Cr with (11CrTi) and without Ti (11Cr) stabilization;
- 16%wt Cr with (16CrNb) and without Nb (16Cr) stabilization;
- For comparative purposes, one austenitic stainless steel with 18%wt Cr and 8%wt Ni (18Cr8Ni) and one carbon steel with 0.15%wt C (ASTM A36).

Their chemical composition is presented in **Table 1**. Moreover, the specimens were thoroughly characterized in terms of mechanical properties and microstructure, details can be found in [36]. **Table 2** summarizes the main mechanical properties of the ferritic stainless steel.

The specimens were characterized in terms of corrosion, microabrasion and microabrasion-corrosion. Potentiodynamic curves were obtained for three test conditions. The first involved pure corrosion tests following the standard ASTM G5-94 [23]. The second involved modified corrosion tests in a turbulent and aerated medium. The third involved microabrasion corrosion tests.

The potentiodynamic curves obtained for the three different test conditions are exemplified in **Figure 10**. All the stainless steel specimens showed regions of cathodic behavior, anodic behavior, passive behavior and transpassive behavior. As expected, the carbon steel (A36) did not show a clear passive behavior (**Figure 10g**).

Comparing the standard corrosion tests with the corrosion tests using aerated conditions, it is possible to observe a substantial increase in the passivation current density (I_p) for all the materials tested. This suggests that the mechanical effect of the turbulence generated by pumping the solution rendered passivation more difficult.

This effect of aerated environments was observed for the corrosion of stainless steel in NaCl solutions by Qiao et al. [43] and by Le Bozec et al. [44] in saturated solutions of oxygen. The latter [44] found that under conditions of oxygen saturation, the anodic and cathodic reactions were accentuated. There is an increase in mass transport by oxygen, accelerating the corrosive process [45]. For the microabrasion-corrosion tests, I_p was further increased, attributable to the abrasion component, which removes the passive film.

Material	YS 0.2% (MPa)	TS (MPa)	El (%)	HV_{10} (MPa)
11Cr	323.8 ± 5.7	411.6 ± 2.0	37.7 ± 0.7	1510 ± 13
11CrTi	316.3 ± 4.1	400.1 ± 1.1	40.4 ± 1.9	1435 ± 11
16Cr	343.1 ± 3.9	488.3 ± 2.9	31.3 ± 1.8	1630 ± 29
16CrNb	336.2 ± 3.3	446.8 ± 1.7	35.9 ± 1.7	1514 ± 15
17CrTiNb	361.3 ± 1.4	483.2 ± 0.8	36.2 ± 0.2	1734 ± 15
18Cr8Ni	347.3 ± 9.4	706.2 ± 7.1	62.3 ± 1.2	1992 ± 9
A36	305.3 ± 4.2	444.8 ± 3.2	34.1 ± 1.0	1358 ± 11

Table 2. Mechanical properties of the specimens; YS = yield strength; TS = tensile strength; El = elongation; HV_{10} = Vickers hardness under 10 kgf normal load.

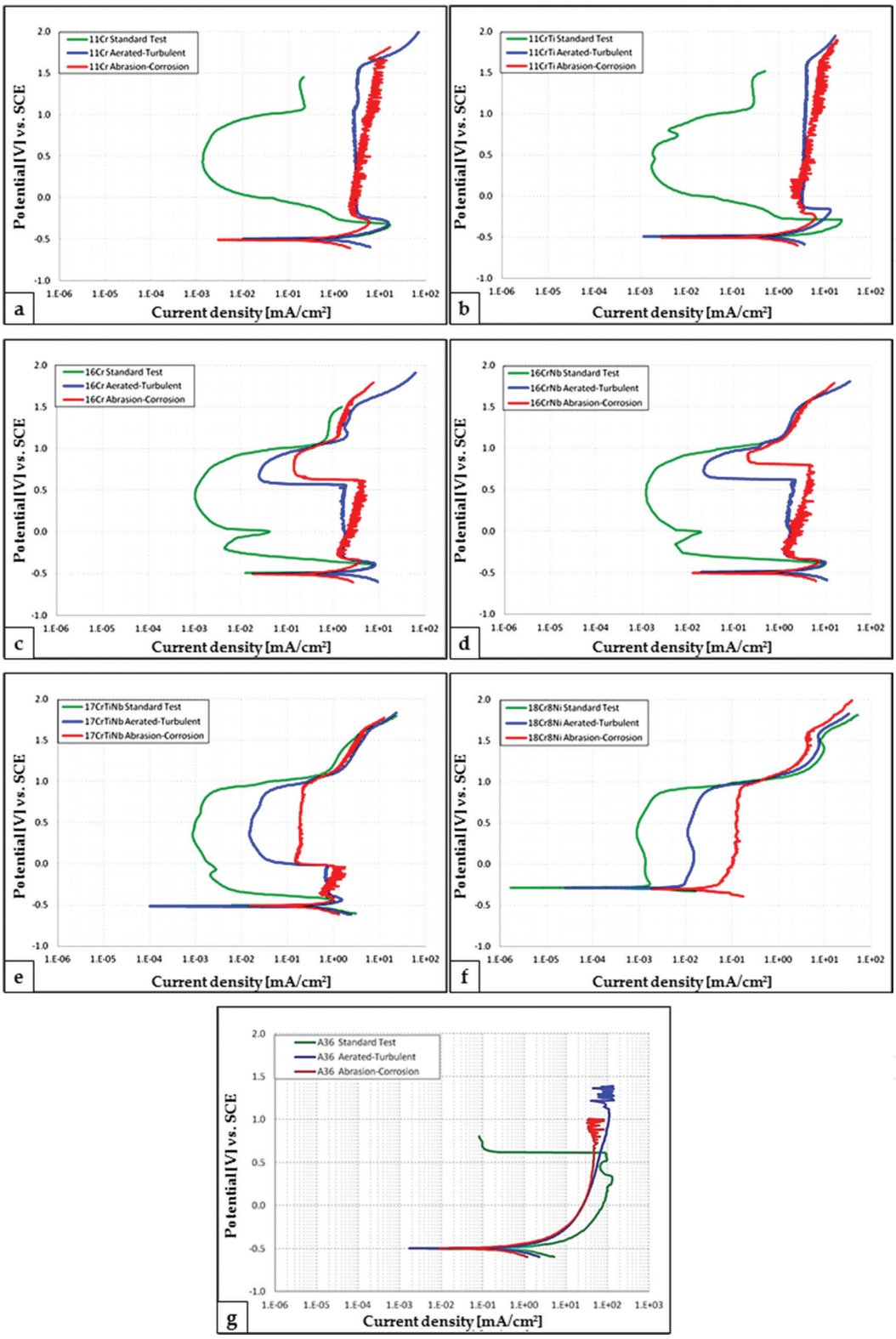

Figure 10. Polarization curves obtained for the three test conditions: (i) standard tests based on ASTM G5-94 (2004); (ii) aerated and turbulent corrosion conditions; and (iii) microabrasion-corrosion tests: (a) 11Cr, (b) 11CrTi, (c) 16Cr, (d) 16CrNb, (e) 17CrTiNb, (f) 18Cr8Ni, (g) A36.

On the other hand, additional interesting features could be observed for the polarization curves obtained under non-standard conditions. For steel with approximately 11% Cr (11Cr and 11CrTi, independently of stabilization), the potentiodynamic curves obtained in the microabrasion-corrosion condition did not show a regular passivation current density plateau; instead, I_p increased slightly but steadily with the potential (**Figure 10a** and **b**). Various authors [4, 40, 41] discuss this increase in passivation current density Ip as a result of the competition between the removal of the passive layer and repassivation. In fact, since it is not an effective passivation, it has been referred to as pseudo-passivation.

When the amount of Cr in the stainless steel increased to 16% (16Cr and 16CrNb, **Figure 10c** and **d**), the aerated tests presented a pseudo-passivation region for lower potentials (between around −400 mV and + 550 mV). After that, a secondary passivation led the current density to stabilize at lower values. Under microabrasion-corrosion conditions, in the pseudo-passive region, the current density again increased slightly with the potential. The secondary passivation still occurred, but at higher potentials. Increasing further the amount of Cr to 17% (**Figure 10e**), the pseudo-passive region and the secondary passivation region were still present for the aerated and microabrasion-corrosion conditions, but the potential for secondary passivation reduced, that is, the mechanical effects influenced less the electrochemical behavior of the material. Aerated conditions increased the passivation current, which was further increased under microabrasion-corrosion conditions.

The reference austenitic stainless steel (**Figure 10f**) with 18%Cr and 8%Ni did not present a pseudo-passive region for the non-standard tests. The current density remained constant during the passive plateau, but again, the agitation of the fluid increased the passivation current and agitation + rubbing increased it further.

The values of passivation current are summarized in **Figure 11**. For the lower Cr content (11%), the passivation currents in fact referred to a pseudo-passive behavior. First (**Figure 11**) shows that, as expected, an increase in the amount of Cr reduced the passivation current, for all the conditions tested. The increase in chromium content tends to accentuate the chemical adsorption through covalent coordinate bonds between the chromium and sulfur (S) atoms in the group of SO_4^{-2}. This fact is in agreement with molecular dynamic simulations by Diawara et al. [46], where the stability of the passive film grows from with Cr content, reaching its maximum at 20% Cr. It is also notorious, the increase in passivation current density I_p with the increase of the intensity of the mechanical event on the surface, first by agitation and then by abrasion.

Another factor that influences the increase of the passive current density in abrasion-corrosion tests is the application and/or increase of the normal force and plastic deformation on the surface of a body in passivation state [10, 42–44]. Ferritic stainless steel samples were subjected to fatigue by means of a servo-hydraulic "Schenck" machine at room temperature applying a load of 40 KN at frequencies of 0.1 and 0.5 Hz in environments of 1 M H_2SO_4 and 0.6 M NaCl [44]. In this test, potentiostatic conditions were imposed using a saturated silver electrode as reference and an exposed area of 3 × 7 mm^2. It was observed that current

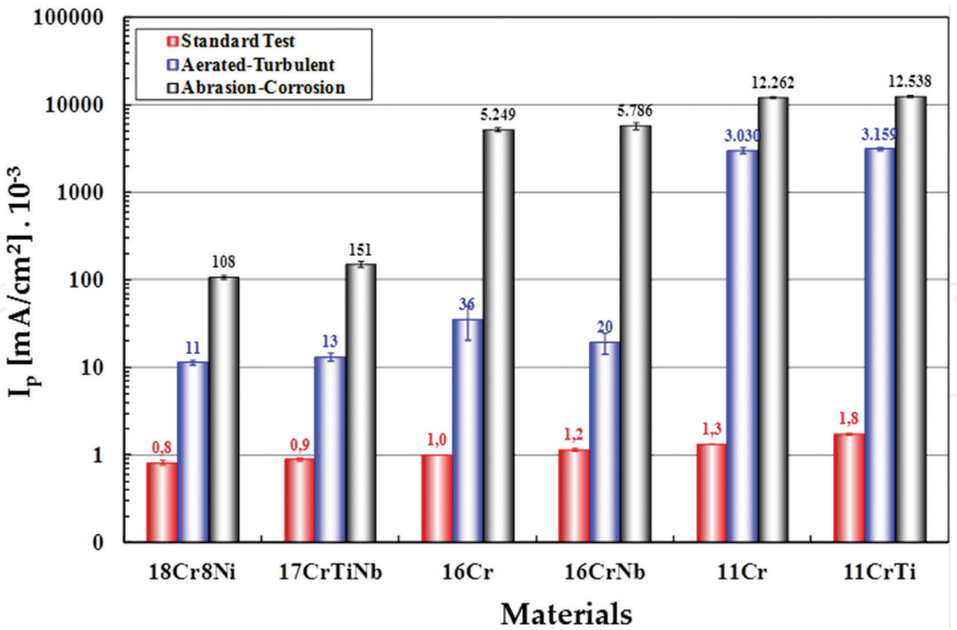

Figure 11. Results of passivation current density for the stainless steel specimens under the three conditions [47].

density increased with the rupture of the passive film due to plastic deformation, and it reduced again after the regeneration of the film on the virgin surface exposed to the corrosive environment. It is worth mentioning that the main difference between low and high frequencies is the time of repassivation of the exposed metal surface, that is, the rate of destruction of the passive film in relation to its generation and growth [44]. In the development of abrasion-corrosion maps [43], testing on a fixed-sphere microabrasion test rig using ultra-high molecular weight polyethylene ball with a suitable electrochemical cell in a physiological solution environment (0.9% NaCl and 10% FCS fetal calf serum), it was observed that for a potential in the 200-mV range, the system current doubled when the force changed from 2 to 3 N.

The normal force was varied during potentiodynamic abrasion-corrosion tests within the region where the imposed electrochemical conditions induced passivation [38]. The specimens were AISI 304 stainless steel, for an environment using abrasive particles of silica in 1 N H_2SO_4 solution and a zirconia ball. **Figure 12** shows a typical polarization curve obtained under these conditions.

The test started with an applied normal force of 1.42 N and during the test the force was decreased to 0.50 N. After 6 min, the load returned to 1.42 N. It is evident that when the force was reduced (from 1.5 to 0.5 N), the passivation current decreased, so the removal of the passive layer was more effective at higher loads [38]. The load variation also induced a change in friction coefficient (**Figure 13**).

In **Figure 13**, it is observed that when the normal force is reduced, the friction coefficient also reduces. The passive layer of the abrasive-corrosive process has lubricating properties, and with lower forces, the passive layer remains more constant and regenerates more efficiently.

http://dx.doi.org/10.5772/intechopen.81913

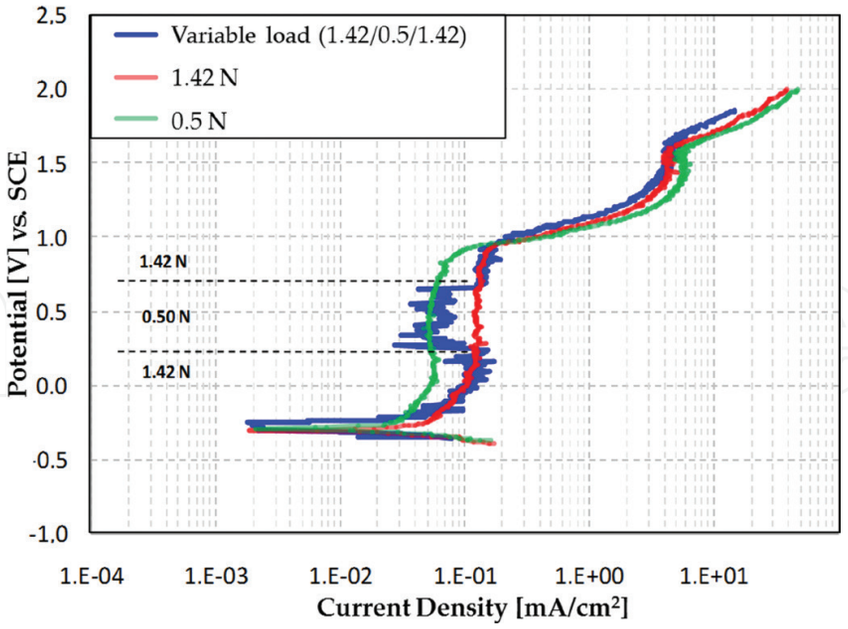

Figure 12. Polarization curves for an abrasion-corrosion test on AISI 304 with variable normal load [10].

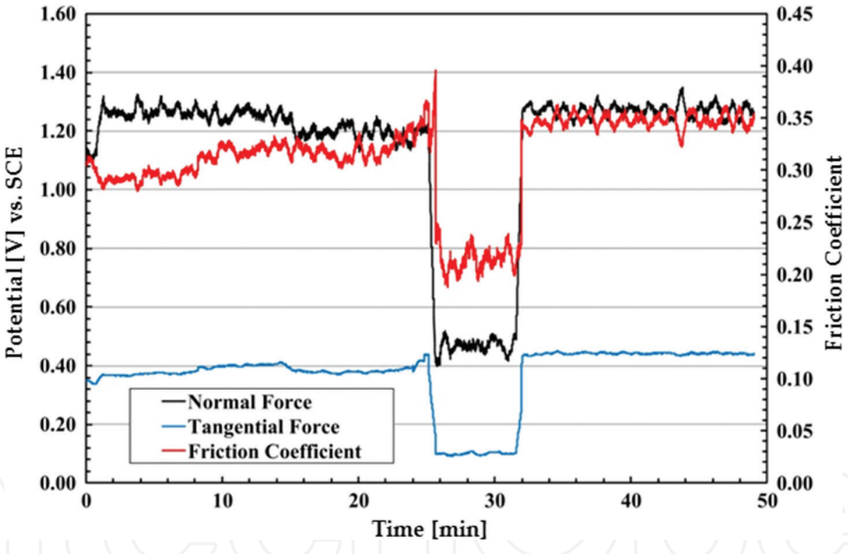

Figure 13. Evolution of contact forces for an abrasion-corrosion test on AISI 304 with variable normal load [10].

The formation of $FeSO_4$ in tribocorrosive systems containing sulfuric acid is the main factor responsible for the reduction of the friction coefficient [48]. Corrosion tests during reciprocal sliding of iron also showed a decrease in friction coefficient when sliding in H_2SO_4 solutions as compared to pure sliding tests using water [49]. In the presence of a H_2SO_4 solution as electrolyte, iron dissolution leads to the formation of $FeSO_4$ on the metallic surface, as indicated by the reaction shown in Eq. (1).

$$Fe_{(s)} + H_2SO_{4(aq)} \rightarrow FeSO_{4(aq)} + H_{2(g)} \quad (1)$$

To show the existence of the $FeSO_4$ film, a sample of ferritic stainless steel 410D (11Cr) was exposed to a 1 N H_2SO_4 solution for 1 hour, and then subjected to Fourier transform infrared spectroscopy (FTIR) analysis (**Figure 14**).

The FTIR spectrum identified humidity bands in the region between 3570 and 2940 cm^{-1} and 1650 cm^{-1}, and more importantly, it confirmed the formation of $FeSO_4$ in the region between 1168 and 1068 cm^{-1} [36].

To verify the kinetics response of the effects of corrosion on friction coefficient, two further test sequences were carried out (**Figure 15**).

In the first (**Figure 15a**), the abrasion-corrosion test was initiated using a water-based abrasive slurry, which was then changed to an abrasive slurry in 1 N H_2SO_4 solution. In the second (**Figure 15b**), the abrasion corrosion test started to use abrasive slurry in 1 N H_2SO_4 solution, which was changed to the abrasive slurry in water. Both curves show a short interval between the two situations, which corresponds to the time required to remove the load and change the slurry. When H_2SO_4 was added to the suspension (**Figure 15a**), the film appeared to form very rapidly, reducing the friction coefficient. In **Figure 15b**, abrasion removed the film, which was not restored in the absence of H_2SO_4, causing increased friction [36].

When comparing the friction coefficients measured during abrasion tests and abrasion-corrosion tests in 1 N H_2SO_4 environment (**Figure 16a**), the influence of the $FeSO_4$ film is evidenced.

The friction coefficient is two times higher in the abrasion tests when compared to the abrasion-corrosion tests. The reduction of friction coefficient under microabrasion-corrosion conditions decreases the amount of mechanical energy that is dissipated in the active interface in the form of friction [36]. This influence is also reflected in the wear coefficient (k). The wear coefficient is substantially lower (3–8 times lower) under abrasion-corrosion conditions when compared to pure abrasion conditions (**Figure 16b**). This behavior was also observed using NaCl solutions

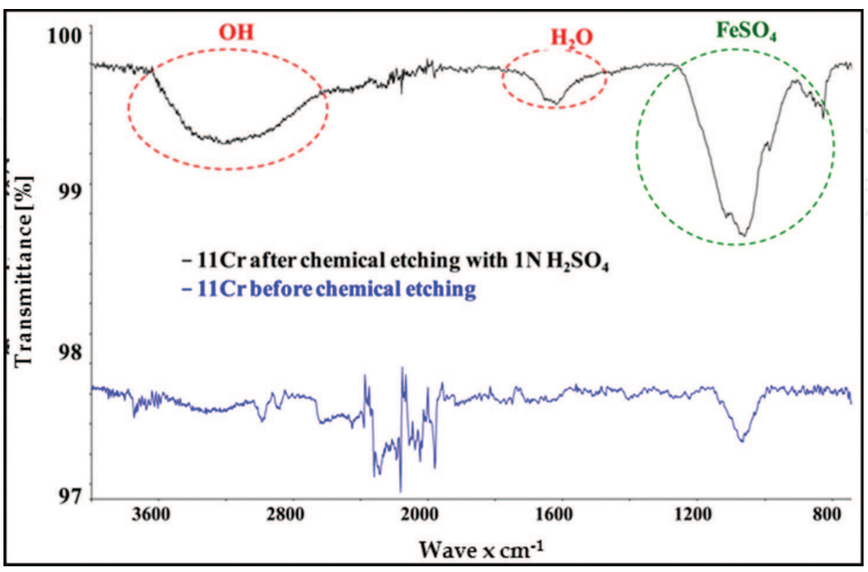

Figure 14. FTIR analysis of 11Cr ferritic stainless steel before and after immersion in 1 N H_2SO_4 solution [15].

http://dx.doi.org/10.5772/intechopen.81913

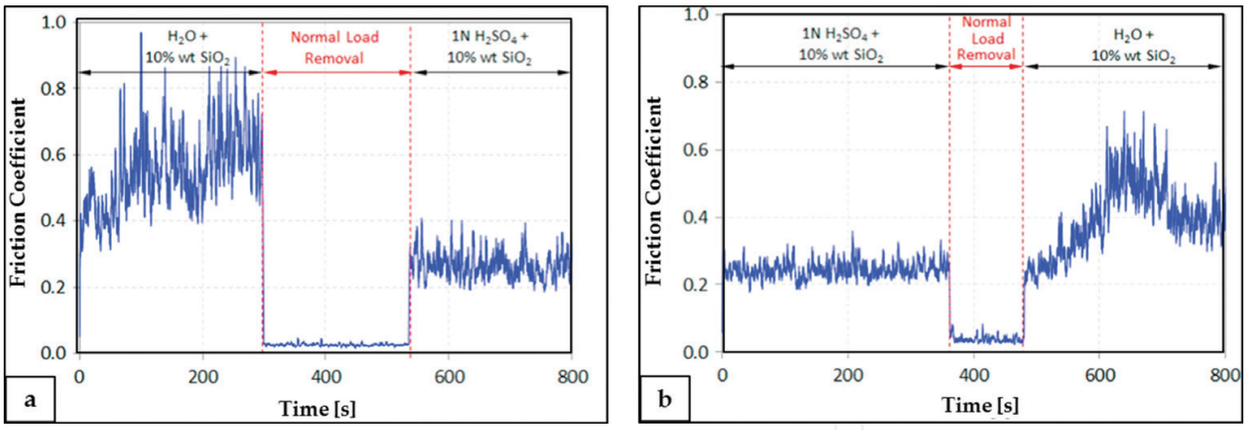

Figure 15. Friction coefficients measured during microabrasion-corrosion tests of 18Cr8Ni: (a) started with water slurry and replaced by 1 N H_2SO_4 slurry; (b) started with 1 N H_2SO_4 slurry and replaced by water slurry [36].

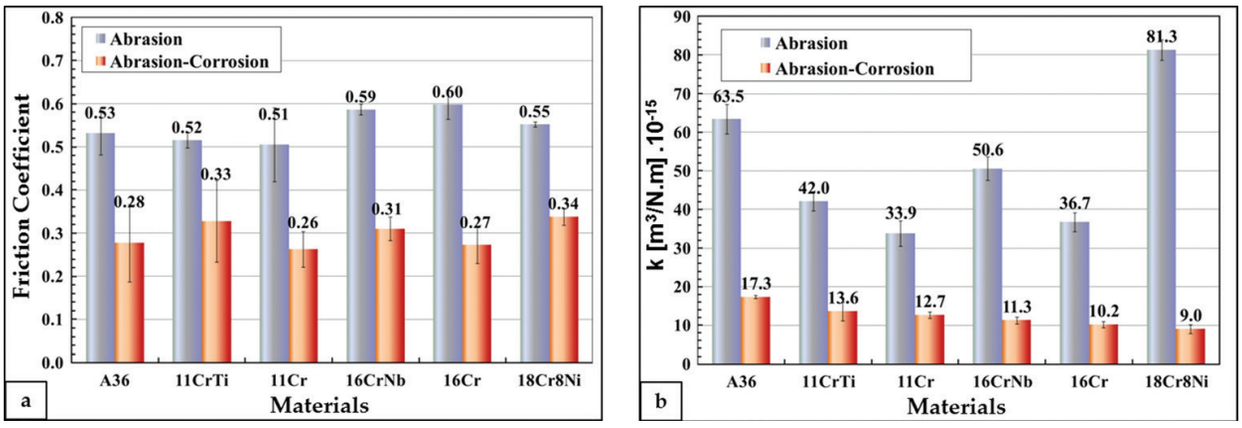

Figure 16. Evaluation of: (a) friction coefficient and (b) wear rate coefficient k, in pure microabrasive and microabrasive-corrosive environment [36].

for AISI 304 stainless steel and AISI 1045 carbon steel [37, 50]. This behavior is associated with the change in repassivation kinetics due to the presence of the corrosive medium and to the external application of a potential difference and the nature of the passive layer [36].

The comparative behavior between the different materials was very different from that observed under pure abrasion conditions, where the austenitic stainless steel had presented the worst performance. Under abrasion-corrosion conditions, the increase in chromium content resulted in a steady reduction of the wear coefficient. Higher Cr contents increase the stability of the passive film in more corrosive environments [28]. Under abrasion-corrosion conditions, the passive film stability seems to govern the behavior of stainless steel [7, 13]. The increase in Cr content could improve the film stability by either hindering depassivation or by accelerating repassivation [36]. The exact mechanism still needs to be elucidated and should be a niche of further research.

The lower wear rates are evidenced in the appearance of wear scars (**Figure 17**). For the two tests, abrasion and abrasion-corrosion arrangements, the predominance of the grooving mechanism is noted. This process occurs in the microscale abrasion test when a significant proportion of the particles slide at the interface producing a series of thin and parallel grooves

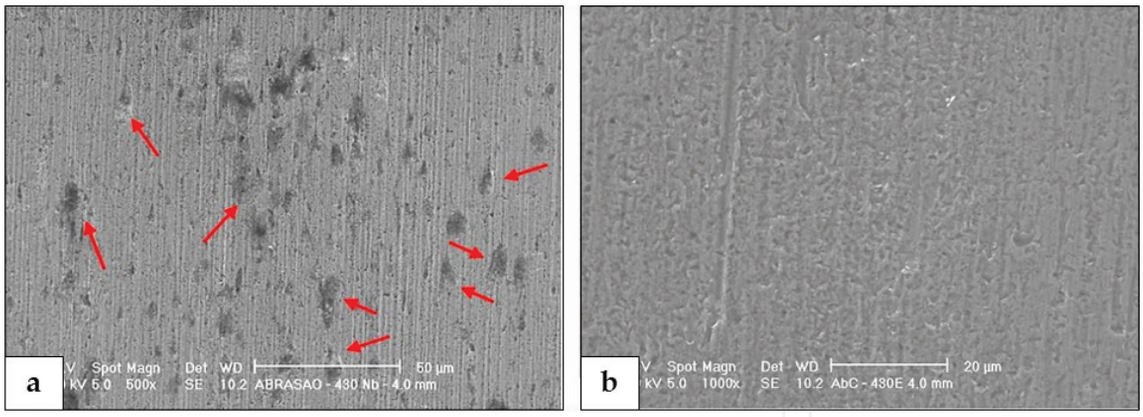

Figure 17. Analysis by SEM of the surfaces of 16CrNb ferritic stainless steel samples after wear testing: (a) microabrasion and (b) microabrasion-corrosion test [52].

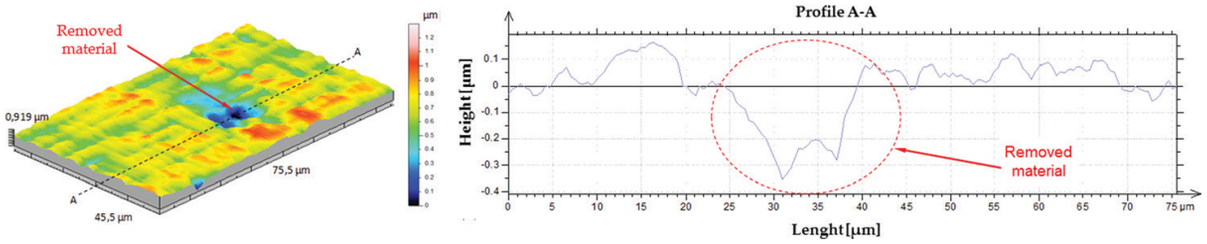

Figure 18. Topographic analysis of the abrasion wear craters evidencing large portions of material removal [17].

on the surface of the sample [51]. **Figure 17** shows that abrasion-corrosion leads to the formation of a significantly smoother surface, which results in less friction [38]. In this way, the smoother surface of abrasion-corrosion (**Figure 17b**) was observed in relation to microabrasion (**Figure 17a**), as a consequence of the low coefficient of friction [38].

The detachment of large portions of material is noteworthy for microabrasion tests (**Figure 17a**), indicated by arrows. Similar localized removal did not occur for the microabrasion-corrosion tests (**Figure 17b**), which showed lower wear coefficients than the carbon steel and the austenitic stainless steel. A 3D topographic assessment of the worn surfaces by laser interferometry (**Figure 18**) confirms that the regions indicated by arrows correspond indeed to areas with intense material removal.

The reduction of friction coefficient under abrasion-corrosion conditions decreases the amount of mechanical energy that is dissipated at the active interface in the form of friction. Vickers microhardness measurements were performed within the wear scars for all materials tested under conditions of pure microabrasion and abrasion-corrosion. The results are shown in **Figure 19**.

According to **Figure 19**, all materials showed an increase in hardness after testing as compared to the microhardness of the samples prior to testing. Strain hardening is a common phenomenon during metal abrasion and has been widely reported in the literature [53, 54]. However, stress hardening was less intense under abrasion-corrosion conditions than under abrasion conditions.

http://dx.doi.org/10.5772/intechopen.81913

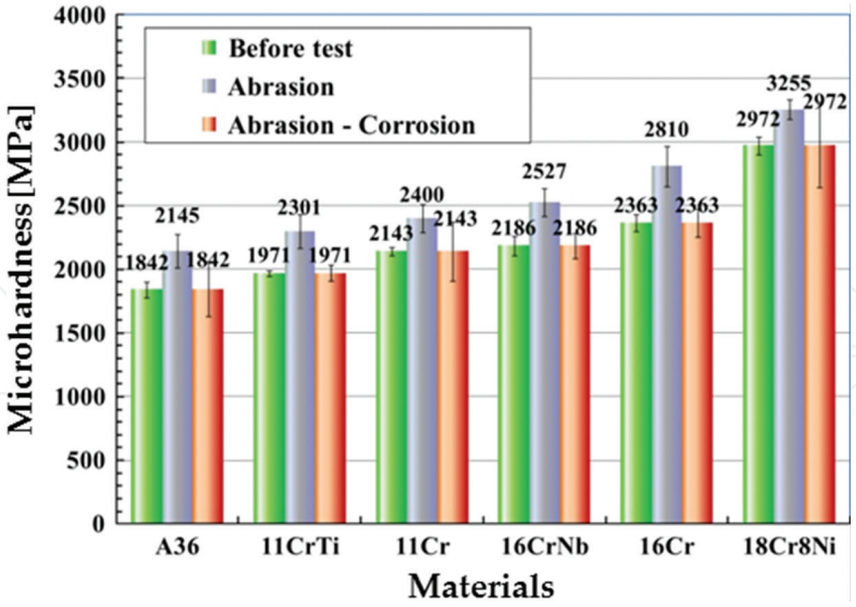

Figure 19. Micro hardness Vickers $HV_{0,05}$ measured within the wear scar before and after microabrasion and microabrasion-corrosion test [36].

Comparing pure microabrasion, which is mechanically dominated, with abrasion-corrosion, use of less energy in mechanical phenomena such as stress hardening was observed. This is in accordance with the lower values of friction coefficient measured under abrasion-corrosion than under pure abrasion, since abrasion-corrosion only needs friction energy for the mechanical removal of passive film, but not for the tribocorrosion of the active areas [36].

5. Conclusions

The main focus of this chapter was the introduction and performance assessment of ferritic stainless steel as an economical option, in particular, under abrasion-corrosion conditions. The comprehensive analysis for situations where pure corrosion, pure abrasion and simultaneous abrasion-corrosion occur allowed to conclude that:

- Particular emphasis was given to the initial stages of sugar cane processing: The ferritic stainless steel, despite its lowest price, showed wear resistance superior to that of more expensive austenitic stainless steel. This resulted in a further investigation of the performance of the ferritic stainless steel when compared to low-carbon steel in a pilot study in three industrial plants. With the successful results obtained with the pilot substitution of some parts that were conventionally manufactured using carbon steel by similar parts in stainless steel, which started in 2003, this substitution increased, so that since 2007 almost all parts in the initial stages of sugar cane processing in the main Brazilian industrial plants have been manufactured using 11Cr stainless steel.
- Both crystallographic texture and Nb/Ti stabilization exerted a strong influence on the corrosion of ferritic stainless steel. Local corrosion (pitting) exhibited an anisotropic behavior and

was influenced by the crystallographic texture, particularly concerning the pitting potential. This anisotropic behavior showed that the presence of the Goss shear texture (oriented along <100>) had a positive influence on the corrosion resistance. Ti and Nb stabilization helped to protect against intergranular corrosion, as the grain borders become less reactive.

- A substantial difference in wear rate, friction coefficient and passive current density was observed for tests performed under different configurations (i.e., corrosion, abrasion and abrasion-corrosion).
- Although the austenitic stainless steel (18Cr8Ni), with the highest Cr content among the materials tested, showed the worst performance under pure abrasion conditions, it presented the best performance in the microabrasion-corrosion tests. Under abrasion-corrosion conditions, the tribological performance improved with the increase in Cr content. The mechanical effects of turbulence and abrasion accelerated the corrosion process, mainly evidenced by an increase in the passivation current density.
- For the abrasion-corrosion tests, a negative synergy was observed. For this configuration, an increase in contact force produced an increase in passive current density. Tests with variable normal force gave a clear indication that this behavior is reversible. The test rig allowed the measurement of friction coefficients during microabrasion tests. This allowed to detect a reduction in friction coefficient during abrasion-corrosion conditions when compared with pure abrasion tests. Friction reduction was attributed to the presence of $FeSO_4$ as a corrosion product, which was confirmed by FTIR analysis.
- Microhardness Vickers measurements inside the wear scars showed a less intense strain hardening under abrasion corrosion conditions than under pure abrasion conditions. This is probably due to the reduction in the energy dissipated as friction in the contact and therefore available for plastic deformation.

Author details

Wilian S. Labiapari[1,2], Miguel A. N. Ardila[1], Henara L. Costa[1,3] and José Daniel B. de Mello[1]*

*Address all correspondence to: ltm-demello@ufu.br

1 Federal University of Uberlândia, Uberlândia, Brazil

2 Aperam South America, Timóteo, Brazil

3 Federal University of Rio Grande, Rio Grande, Brazil

References

[1] Stack MM, Chi K. Mapping sliding wear of steels in aqueous conditions. Wear. 2003;**255**:456-465

[2] Stack MM, Jawan H, Mathew MT. On the construction of micro-abrasion maps for a steel/polymer couple in corrosive environments. Tribology International. 2005;**38**:848-856

[3] Labiapari WS, Alcântara CM, Costa HL, de Mello JDB. Stainless steel as an antiwear material for the bio-fuel industry. Wear. 2013;**302**:1536-1545

[4] Wood RJK, Sun D, Thakare MR, de Frutos Rozas A, Wharton JA. Interpretation of electrochemical measurements made during micro-scale abrasion-corrosion. Tribology International. 2010;**43**:1218-1227

[5] Landolt D, Mischler S, Stemp M, Barril S. Third body effects and material fluxes in tribo-corrosion systems involving a sliding contact. Wear. 2004;**256**:517-524

[6] Bello JO, Wood RJK, Wharton JA. Synergistic effects of micro-abrasion–corrosion of UNS S30403, S31603 and S32760 stainless steels. Wear. 2007;**263**:149-159

[7] Gant AJ, Gee MG, May AT. The evaluation of tribo-corrosion synergy for WC–Co hard-metals in low stress abrasion. Wear. 2004;**256**:500-516

[8] Sun D, Wharton JA, Wood RJK. Micro-abrasion mechanisms of cast CoCrMo in simulated body fluids. Wear. 2009;**267**:1845-1855

[9] Thakare MR, Wharton JA, Wood RJK, Menger C. Exposure effects of strong alkaline conditions on the microscale abrasion–corrosion of D-gun sprayed WC–10Co–4Cr coating. Tribology International. 2008;**41**:629-639

[10] ANFAVEA, Monthly Report, Associacão Nacional dos Fabricantes de Veículos Automotores Brazil; 2012

[11] Volci GA. Comportamento tribológico do anel de primeiro canalete em motores operando em sistemas flex fuel, Mechanical Engineering. Brazil: UFPR; 2007. p. 116

[12] Cheng YF, Bullerwell J, Steward FR. Electrochemical investigation of the corrosion behavior of chromium-modified carbon steels in water. Electrochimica Acta. 2003;**48**:1521-1530

[13] Dobbelaar JAL, Herman ECM, de Wit JHW. The corrosion behaviour of iron-chromium alloys in 0.5 M sulphuric acid. Corrosion Science. 1992;**33**:765-778

[14] Huh MY, Lee JH, Park SH, Engler O, Raabe D. Effect of through-thickness macro and micro-texture gradients on ridging of 17% Cr ferritic stainless steel sheet. Steel Research International. 2005;**76**:797-806

[15] Hutchinson B. Deformation microstructures and textures in steels. Philosophical Transactions of the Royal Society of London A: Mathematical, Physical and Engineering Sciences. 1999;**357**:1471-1485

[16] Kumar BR, Singh AK, Das S, Bhattacharya DK. Cold rolling texture in AISI 304 stainless steel. Materials Science and Engineering A. 2004;**364**:132-139

[17] Raabe D, Lücke K. Influence of particles on recrystallization textures of ferritic stainless steels. Steel Research. 1992;**63**:457-464

[18] Raabe D, Lücke K. Texture and microstructure of hot rolled steel. Scripta Metallurgica et Materialia. 1992;**26**:1221-1226

[19] Raabe D, Lüucke K. Textures of ferritic stainless steels. Materials Science and Technology. 1993;**9**:302-312

[20] Raabe D, Reher F, Hölscher M, Lücke K. Textures of strip cast Fe16% Cr. Scripta Metallurgica et Materialia. 1993;**29**:113-116

[21] Ardila MAN, Labiapari WS, De Mello JDB. The influence of crystallographic texture and niobium stabilisation on the corrosion resistance of ferritic stainless steel. Materials Research. 2017;**20**:576-583

[22] Siqueira RP, Sandim HRZ, Oliveira TR, Raabe D. Composition and orientation effects on the final recrystallization texture of coarse-grained Nb-containing AISI 430 ferritic stainless steels. Materials Science and Engineering A. 2011;**528**:3513-3519

[23] ASTM. Standard Test Method for Conducting Potentiodynamic Polarization Resistance Measurements. West Conshohocken, PA: ASTM International; 1991. pp. G59-G97

[24] Huang C, Zou B, Liu Y, Zhang S, Huang C, Li S. Study on friction characterization and wear-resistance properties of Si3N4 ceramic sliding against different high-temperature alloys. Ceramics International. 2016;**42**:17210-17221

[25] Ma L, Hu S, Shen J, Han J, Zhu Z. Effects of Cr content on the microstructure and properties of 26Cr–3.5Mo–2Ni and 29Cr–3.5Mo–2Ni super ferritic stainless steels. Journal of Materials Science and Technology. 2016;**32**:552-560

[26] Hamdy AS, El-Shenawy E, El-Bitar T. The corrosion behavior of niobium bearing cold deformed austenitic stainless steels in 3.5% NaCl solution. Materials Letters. 2007;**61**:2827-2832

[27] Kiminami CS, Souza CAC, Bonavina LF, de Andrade Lima LRP, Suriñach S, Baró MD, et al. Partial crystallization and corrosion resistance of amorphous Fe-Cr-M-B (M=Mo, Nb) alloys. Journal of Non-Crystalline Solids. 2010;**356**:2651-2657

[28] Koga GY, Nogueira RP, Roche V, Yavari AR, Melle AK, Gallego J, et al. Corrosion properties of Fe–Cr–Nb–B amorphous alloys and coatings. Surface and Coatings Technology. 2014;**254**:238-243

[29] Sousa CAC, Kuri SE. Relationship between niobium content and pitting corrosion resistance in ferritic stainless steels. Materials Letters. 1995;**25**:57-60

[30] Davis BW, Moran PJ, Natishan PM. Metastable pitting behavior of aluminum single crystals. Corrosion Science. 2000;**42**:2187-2192

[31] Park SY, Kim JH, Lee MH, Jeong YH. Effects of the microstructure and alloying elements on the iodine-induced stress-corrosion cracking behavior of nuclear fuel claddings. Journal of Nuclear Materials. 2008;**376**:98-107

[32] Shahryari A, Szpunar JA, Omanovic S. The influence of crystallographic orientation distribution on 316LVM stainless steel pitting behavior. Corrosion Science. 2009;**51**:677-682

[33] Kruger J. Influence of crystallographic orientation on the pitting of iron in distilled water. Journal of the Electrochemical Society. 1959;**106**:736

[34] Guo WY, Sun J, Wu JS. Effect of deformation on corrosion behavior of Ti–23Nb–0.7Ta–2Zr–O alloy. Materials Characterization. 2009;**60**:173-177

[35] Costa HL, Ardila MAN, Labiapari WS, Silva WM, de Mello JDB. Effect of surface topography on the dynamics of the abrasive particles during micro-abrasion. Wear. 2015;**324-325**:129-139

[36] Labiapari WS, Ardila MAN, Costa HL, de Mello JDB. Micro abrasion-corrosion of ferritic stainless steels. Wear. 2017;**376-377**(Part B):1298-1306

[37] Oltra R, Chapey B, Renaud L. Abrasion-corrosion studies of passive stainless steels in acidic media: Combination of acoustic emission and electrochemical techniques. Wear. 1995;**186-187**:533-541

[38] Santos MB, Labiapari WS, Ardila MAN, da Silva WM, de Mello JDB. Abrasion–corrosion: New insights from force measurements. Wear. 2015;**332-333**:1206-1214

[39] Sinnett-Jones PE, Wharton JA, Wood RJK. Micro-abrasion–corrosion of a CoCrMo alloy in simulated artificial hip joint environments. Wear. 2005;**259**:898-909

[40] Stack MM, Zhou S, Newman RC. Identification of transitions in erosion-corrosion regimes in aqueous environments. Wear. 1995;**186-187**:523-532

[41] Ferrer F, Idrissi H, Mazille H, Fleischmann P, Labeeuw P. A study of abrasion–corrosion of AISI 304L austenitic stainless steel in saline solution using acoustic emission technique. NDT and E International. 2000;**33**:363-371

[42] Mischler S, Rosset E, Stachowiak GW, Landolt D. Effect of sulphuric acid concentration on the rate of tribocorrosion of iron. Wear. 1993;**167**:101-108

[43] Qiao YX, Zheng YG, Okafor PC, Ke W. Electrochemical behaviour of high nitrogen bearing stainless steel in acidic chloride solution: Effects of oxygen, acid concentration and surface roughness. Electrochimica Acta. 2009;**54**:2298-2304

[44] Le Bozec N, Compère C, L'Her M, Laouenan A, Costa D, Marcus P. Influence of stainless steel surface treatment on the oxygen reduction reaction in seawater. Corrosion Science. 2001;**43**:765-786

[45] Freguia S, Rabaey K, Yuan Z, Keller J. Non-catalyzed cathodic oxygen reduction at graphite granules in microbial fuel cells. Electrochimica Acta. 2007;**53**:598-603

[46] Diawara B, Beh YA, Marcus P. Atomistic Simulation of the Passivation of Iron-Chromium Alloys Using Calculated Local Diffusion Activation Barriers; 2006

[47] Labiapari WS, Ardila MAN, Costa HL, de Mello JDB. Mechanical Effects on the Corrosion Resistance of Ferritic Stainless Steels During Microabrasion-Corrosion, Wear of Materials (WOM), Wear, Miami; 2019

[48] Kolesnichenko LF, Trushko PV. Formation of boundary layers during friction in the presence of sulfur. Soviet Powder Metallurgy and Metal Ceramics. 1970;**9**:993-997

[49] Miyoshi K. Studies of mechanochemical interactions in the tribological behavior of materials. Surface and Coatings Technology. 1990;**43**:799-812

[50] Bateni MR, Szpunar JA, Wang X, Li DY. The effect of wear and corrosion on internal crystalline texture of carbon steel and stainless steel. Wear. 2005;**259**:400-404

[51] Trezona RI, Allsopp DN, Hutchings IM. Transitions between two-body and three-body abrasive wear: Influence of test conditions in the microscale abrasive wear test. Wear. 1999;**225-229**(Part 1):205-214

[52] Labiapari WS. Abrasão-corrosão em aços inoxidáveis ferríticos. Uberlândia: Programa de Pós-graduação em Engenharia Mecânica, Universidade Federal de Uberlândia (UFU); 2015. p. 211

[53] Hutchings IM. Tribology: Friction and Wear of Engineering Materials. London: Edward Arnold; 1992

[54] Zum Gahr KH. Microstructure and Wear of Materials. Amsterdam: Elsevier Science; 1987